SHOCK WAVE LAMINAR BOUNDARY LAYER INTERACTION OVER A DOUBLE WEDGE IN A HIGH MACH NUMBER FLOW

BY MOHAMMAD ALI BADR

A thesis submitted to the

Graduate School—New Brunswick

Rutgers, The State University of New Jersey

in partial fulfillment of the requirements

for the degree of

Master of Science

Graduate Program in Mechanical and Aerospace Engineering

Written under the direction of

Dr Doyle Knight

and approved by

_____

_____

_____

New Brunswick, New Jersey

January, 2016

ABSTRACT OF THE THESIS

Shock Wave Laminar Boundary Layer Interaction Over a Double Wedge in a High Mach Number Flow

by Mohammad Ali Badr

Thesis Director: Dr Doyle Knight

Shock wave laminar boundary layer interaction (SWBLI) over a double wedge was simulated at Mach 7.11 with stagnation enthalpy of 2 MJ/kg (low enthalpy case), and at Mach 7.14 with stagnation enthalpy of 8 MJ/kg (high enthalpy case) using the commercial flow solver GASPex. An inviscid simulation was performed at Mach 7.14 for validation and solution justification. In the inviscid case, the region downstream of the first shock wave shows less than one percent difference for any flow parameter in comparison with oblique shock wave theory. In both cases, the flow is assumed to be laminar. The computed heat transfer distribution agrees closely with the experiment at the time reported by experiment where the flow reaches steady state; however, significant differences are evident in the duration in which the flow reaches steady state in the computation. In particular, the time-accurate simulations indicate a significantly longer physical time to achieve steady state than observed in the experiment.

Keywords: Shock Boundary Layer Interaction, Laminar Flow, Surface Heat Transfer, GASPex

Acknowledgements

First of all, I want to thank Dr. Knight for presenting this problem to me, believing I can conduct this research, and guiding me through the process. When I was told this research is part of a NATO STO task group, and a team of accredited scholars from around the world are contributing to this research, and that a previous attempt was concluded with the agreement of numerical solutions, but not with the experimental, I was excited and motivated.

I want to thank Dr. Reece Neel from Aerosoft who would answer my questions on how to use *GASPex*, technical methods that *GASPex* uses to calculate surface heat transfer, and how to improve my grid generation and reach flow convergence. For running the software, I want to thank Dr. Alexei Kotelnikov who helped me with running *GASPex* on various clusters and machines, including the SOE cluster. Again, I want to thank Dr. Knight who provided me his HPC cluster for as long I needed.

At the end, I want to thank my parents who supported me through my years in Rutgers. Of course, I'm also grateful for their help and support through my life.

Table of Contents

List of Tables

List of Figures

Chapter 1

Introduction

Hypersonic flight is an area of active and intense research. On 1 May 2013, through a combined booster and scramjet propulsion system, the Boeing X-51A successfully flew for the fourth time reaching Mach 5.1. Prior to the X-51, other attempts were taken place by NASA's X-43, University of Queensland's (UQ's) HyShot project and UQ's most recent program, HIFiRE, managed by the Defence, Science and Technology Organisation (DSTO, Australia) and the US Air Force Research Laboratory (AFRL).

A critical issue in the design of hypersonic vehicles is the thermal protection system. Reattaching shear layers can generate extremely high local heat transfer rates, and therefore accurate prediction of surface heat transfer is important. This initiates interest in investigating shock wave boundary layer interaction (SWBLI) in depth and developing high accurate numerical models which are able to predict flow behavior wherever this phenomena occurs.

1.1   Background

The NATO Applied Vehicle Technology Task Group AVT 136, established in 2006, performed a detailed analysis of CFD capability for prediction of surface heat transfer and surface pressure due to laminar shock wave boundary layer interaction in non-equilibrium hypersonic flow [1] . The conclusions were mixed. For the Run 42 experiment in Nitrogen of a $25° - 55°$ double cone at Mach 11.7 and stagnation enthalpy of 9.17 MJ/kg performed at the Calspan University of Buffalo Research Center (CUBRC), the comparison of the predicted and experimental surface pressure and heat transfer from six different CFD codes was very good. For the Run 40 experiment in Nitrogen of the same configuration at 5.38 MJ/kg, the comparison of the predicted and

experimental surface pressure and heat transfer from six different CFD codes was poor.

The NATO Applied Vehicle Technology Task Group AVT 205 was established in 2012 to further assess the capability for prediction of aerothermodynamic heating for hypersonic vehicles. Three experiments were selected. The double wedge configuration of Swantek and Austin [2] was chosen to assess the CFD capability for prediction of surface heat transfer in hypersonic laminar shock wave boundary layer interactions.

SWBLI for laminar and turbulent boundary layers are under investigation for seven decades and dates back to the late 1950's [3]. They occur in internal and external flow configuration, and for speeds varying from transonic to supersonic and hypersonic. Understanding this phenomena and shock structure for various flows, active and passive control of shock formation and flow structure, designing thermal protection and heat shields, understanding pressure fluctuation and flattering, and in a broader view assessment of computational capabilities and numerical accuracy to simulate shock interaction occurrence (which includes understanding and developing new flux algorithms) was under study. This has lead to prototypes for ramjet and scramjet inlets, improved turbojet inlet design that prevents choking while an aircraft maneuvers in supersonic speeds, understanding flow structure (bow shock, lambda shock, slip line, etc.), passive shock weakening techniques like micro ramps, microelectromechanical systems (MEMS), and vortex generators, as well as active flow control such as jet flow and variable nozzle, design of heat shields and ablative material, and finally improvement in test facilities and measurement instruments, and computational strength and flux algorithms [3], [4].

One of the continuing area of research in this field is the modeling of surface heat transfer due to shock wave boundary layer interaction. According to Dolling [4], within the first fifty years of research, computational prediction of surface heat transfer has not been accurate and this topic needs to be investigated. This effort requires accredited experiments to work as test cases so that the numerical solutions could be validated. Salin et $al.$ [5] investigated symmetric $7°$ and $15°$ double-sharp-fin in Mach 3.92 for SWTBLI using Reynolds average Navier-Stokes (RANS) for turbulent models ω-based

Reynolds stress equation (RSE), two-equation shear stress transport (SST), and one-equation eddy viscosity transport (EVT). The computational wall pressure distribution on the centerline for all three models matched well with experimental values. In addition, RSM showed to have best agreement. Wall heat transfer coefficient prediction was improved by using RANS-RSM by 50%, in comparison with two-equation turbulent RANS, and by increasing the Prandtl number by a factor of 10, and by using pressure-correlation based formula. Borovoy *et al.* [6] computed laminar and turbulent SWBLI sharp and blunt plates in Mach 5-10 flow with an undistributed boundary layer for Reynolds 0.3×10^6 and 27×10^6 and reported in the reattachment region that the maximum value of the heat-transfer coefficient is significantly reduced by bluntness. This is due to decreasing of gas density in the high-entropy layer and increasing of the separation-zone length. Rouhi Youssefi and Knight [7] simulated a double cone in Mach 12.2, and 12.84 laminar flow with total enthalpy per unit mass of $5.44MJ/kg$ and $21.77MJ/kg$. Both case where simulated in perfect gas and Park I thermochemistry model. As they reported, although the computational values for surface heat transfer assuming perfect gas matched well for the low enthalpy case, values did not agree for the high enthalpy case, due to thermochemical flow reaction. The real gas model did result in better agreement with experimental values, and in addition a non-catalytic boundary condition at the wall manages to predict separation and reattachment points more accurately than the air catalysis boundary condition at the wall. Patil *et al.* [8] investigated a double wedge in Mach 7.11 and 7.18, and stagnation enthalpies of $2.0MJ/kg^3$ and $8.0MJ/kg^3$ in laminar flow using direct simulation Monte Carlo (DSMC). The computed surface heat transfer with the DSMC matched those of an experiment on the first surface (fore-body), but did not match on the second (aft) wedge. They suggested this could be in part because the averaging of surface heat transfer values that occurs in experiment. For the low enthalpy case, the same conclusion was made. Both cases managed to capture the flow structure the same way the experiment did.

1.2   About The Scope

In the next chapter, the detailed problem statement will be presented, along with the geometry and issues in focus. The method of solution including the grid formation and flux algorithm is introduced in Chapter 4. Results are shown in Chapter 5, and conclusions are presented in Chapter 6.

Chapter 2

Problem Statement

Steady state surface heat transfer, and time to reach steady state, of a double wedge in a hypersonic non-reacting high Mach number flow (Mach 7) is desired. The computational values will be compared with experimental values to assist the CFD capabilities and accuracy. The three dimensional view of the double wedge is shown in Fig. 2.1.

2.1   Experimental Setup

The experimental values for the surface heat transfer are obtained from the University of Illinois' Hypervelocity Expansion Tube (HET) which has a 9.14 m long expansion tube with driver, driven, and accelerator sections. The internal diameter for all sections is 150 mm. The model is machined from A2 tool steel. Nineteen coaxial thermocouples with diameter 2.4 mm and response time 1 μs, are placed on sixteen streamwise locations. Three thermocouples are placed to measure spanwise variations. The error bar due to gauge uncertainties is 8% [2].

2.2   Geometry

The configuration, as illustrated in Fig. 2.2, is a nominally two dimensional double wedge. The total length of model ($L_t = L_f + L_a$) is 58.572 mm and total height ($H_t = H_f + H_a$) is 46.203 mm. A pre-wedge length (L_p) is added to the model for computational purposes, and will be discussed in Section 4.1. The length and inclination angle for the forward and aft wedges are shown in Table 2.1. In both the numerical model and experimental model, a flat surface exists after the second wedge, but has no significant contribution to the heat transfer on the wedge surfaces.
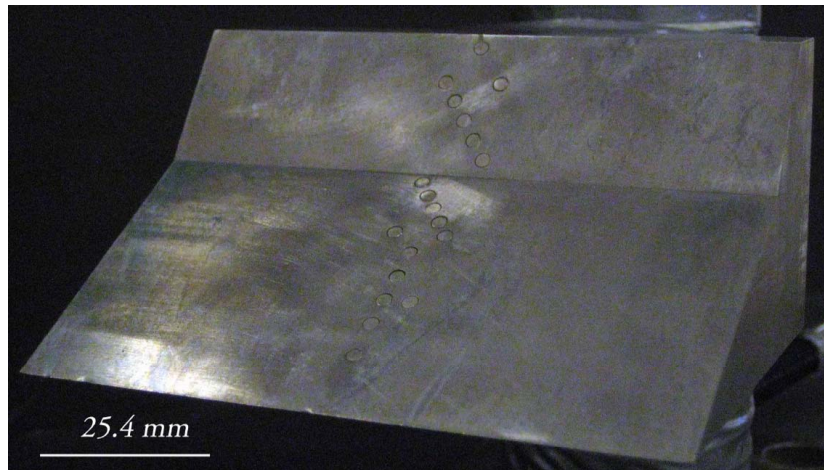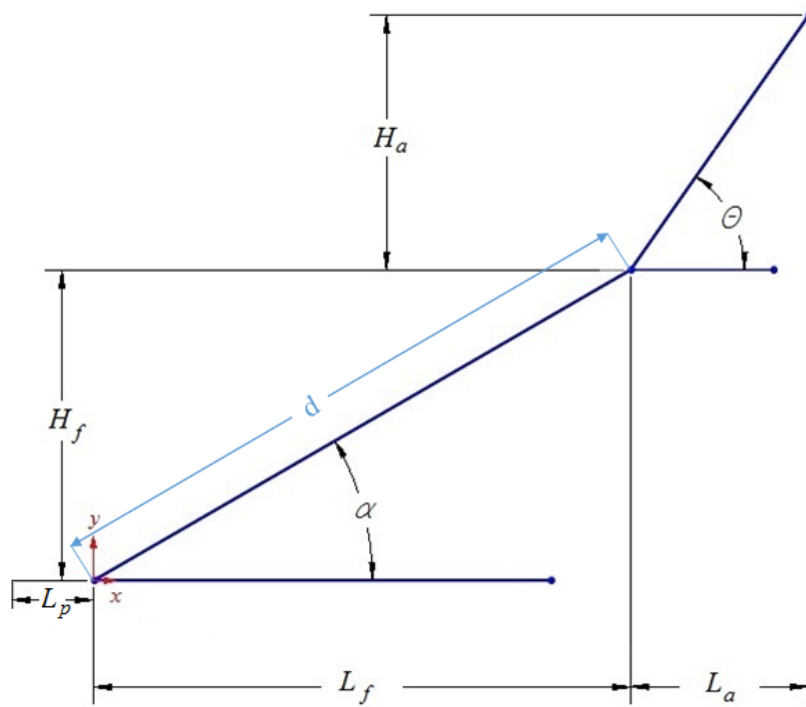
Figure 2.1: Three dimensional object

Figure 2.2: Double wedge characteristics definition

Table 2.1: Double wedge configuration

Definition	Symbol	Value [9]
Pre-wedge length	L_p	10.000 mm
Forward wedge length	L_f	43.993 mm
Aft wedge length	L_a	14.580 mm
Total wedges length	L_t	58.573 mm
Forward wedge height	H_f	25.400 mm
Aft wedge height	H_a	20.803 mm
Total wedges height	H_t	46.203 mm
Forward wedges face length	d	50.799 mm
Forward wedge angle	α	30.0°
Aft wedge angle	θ	55.0°

2.3   Shock Wave Boundary Layer Interaction

The flow conditions[1] are shown in Table 2.2 corresponding to tests M7_2 (low enthalpy) and M7_8 (high enthalpy) in Swantek and Austin [2]. For such flow over the mentioned geometry, shock wave boundary layer interaction is expected to occur on the surface of the double wedge. The forward surface of the double wedge will create an oblique shock and its values for inviscid flow could be verified by NACA report 1135 [10].

2.4   Surface Heat Transfer

By the nature of the experiment, the wall temperature is constant for the duration of the experiment [2]. while the flow temperature rises after the shock wave. This assumption is valid, especially since the run time of the experiment is very short (typically in fractions of a millisecond). This assumption causes conduction heat transfer from the flow (hot) to the wall (cold). As mentioned above, the experiment utilized

---

[1]Where "∞" denotes free stream, and "W" denotes wall values

Table 2.2: Flow properties

Property	Symbol	High Enthalpy	Low Enthalpy
Stagnation enthalpy per Mass	h_o	8.0 $\frac{\text{MJ}}{\text{kg}}$	2.1 $\frac{\text{MJ}}{\text{kg}}$
Mach Number	M	7.14	7.11
Static Pressure	P_∞	780 Pa	391 Pa
Static Temperature	T_∞	710 K	191 K
Velocity	U_∞	3,812 $\frac{\text{m}}{\text{s}}$	1,972 $\frac{\text{m}}{\text{s}}$
Density	ρ_∞	0.0038 $\frac{\text{kg}}{\text{m}^3}$	0.0071 $\frac{\text{kg}}{\text{m}^3}$
Wall Temperature	T_W	298 K	298 K

thermocouples with 8% gauge uncertainty [2].

Chapter 3

Fundamental Equations

This chapter introduces the governing equations in tensor notation and in two-dimensional vector format for Cartesian and curvilinear coordinate system. In order to solve the equations with a finite volume method, the two-dimensional vector equations will be integrated over a cell. Since the derived equations are solved with the VanLeer's flux vector splitting method for the inviscid fluxes, this flux will be discussed. Part of the numerical computation applies reconstruction, thus the modified essentially non-oscillatory (ENO) limiter will be introduced.

3.1   Tensor Form of Governing Equations

The governing equations (using Einstein's summation conservation) for variables described in Table 3.1 are as follows [11] .

Conservation of Mass

$$\frac{\partial \rho}{\partial t} + \frac{\partial \rho u_i}{\partial x_i} = 0$$

Conservation of Momentum

$$\frac{\partial \rho u_i}{\partial t} + \frac{\partial \rho u_i u_j}{\partial x_i} = -\frac{\partial P}{\partial x_i} + \frac{\partial \tau_{ij}}{\partial x_j}$$

$$\tau_{ij} = \mu(\frac{\partial u_j}{\partial x_i} + \frac{\partial u_i}{\partial x_j}) + (\mu_v - \frac{2}{3}\mu)\frac{\partial u_m}{\partial x_m}\delta_{ij}$$

Equation of state

$$P = \rho R T$$

Table 3.1: Flow properties

Symbol	Property	Symbol	Property
R	Gas constant	τ_{ij}	Stress
T	Static temperature	μ	Dynamic viscosity
e	Total energy per unit mass	μ_v	Coefficient of bulk viscosity
κ	Thermal conductivity	$\partial/\partial t$	Time derivative
ρ	Density	$\partial/\partial x_i$	Spatial derivative in i-th direction
P	Pressure	δ_{ij}	Kronecker delta
u_i	Velocity in i-th direction		

Conservation of Energy

$$\frac{\partial \rho e}{\partial t} + \frac{\partial ((P + \rho e) u_i)}{\partial x_i} = \frac{\partial (\tau_{ij} u_j)}{\partial x_i} + \frac{\partial}{\partial x_i}(\kappa \frac{\partial T}{\partial x_i})$$

3.2 Vector Form of Governing Equations

The two-dimensional vector format of the fundamental equations in Cartesian coordinate system is:

$$\frac{\partial Q}{\partial t} + \frac{\partial E}{\partial x} + \frac{\partial F}{\partial y} = \frac{\partial R}{\partial x} + \frac{\partial S}{\partial y}$$

where there is no body force, and u and v are velocity components in x- and y- direction, ρ is density, τ is stress, κ is thermal conductivity, T is temperature, and:

$$Q = \left\{ \begin{array}{c} \rho \\ \rho u \\ \rho v \\ \rho e \end{array} \right\}, E = \left\{ \begin{array}{c} \rho u \\ \rho u^2 + p \\ \rho u v \\ \rho e u + p u \end{array} \right\}, F = \left\{ \begin{array}{c} \rho v \\ \rho v u \\ \rho v^2 + p \\ \rho e v + p v \end{array} \right\}$$

$$R = \left\{ \begin{array}{c} 0 \\ \tau_{xx} \\ \tau_{xy} \\ u\tau_{xx} + v\tau_{xy} + \kappa\frac{\partial T}{\partial x} \end{array} \right\}, S = \left\{ \begin{array}{c} 0 \\ \tau_{xy} \\ \tau_{yy} \\ u\tau_{xy} + v\tau_{yy} + \kappa\frac{\partial T}{\partial y} \end{array} \right\}$$

Transforming to curvilinear coordinate system $\xi(x,y), \eta(x,y)$ yields:

$$\frac{\partial Q'}{\partial t} + \frac{\partial E'}{\partial \xi} + \frac{\partial F'}{\partial \eta} = \frac{\partial R'}{\partial \xi} + \frac{\partial S'}{\partial \eta}$$

$$Q' = \frac{1}{J} \left\{ \begin{array}{c} \rho \\ \rho u \\ \rho v \\ \rho e \end{array} \right\}, u' = \xi_x u + \xi_y v, v' = \eta_x u + \eta_y v, J = \frac{\partial(\xi,\eta)}{\partial(x,y)} = (\frac{\partial x}{\partial \xi}\frac{\partial y}{\partial \eta} - \frac{\partial y}{\partial \xi}\frac{\partial x}{\partial \eta})^{-1}$$

$$E' = \frac{1}{J} \left\{ \begin{array}{c} \rho u' \\ \rho u u' + \xi_x p \\ \rho v u' + \xi_y p \\ (\rho e + p)u' \end{array} \right\}, F' = \frac{1}{J} \left\{ \begin{array}{c} \rho v' \\ \rho u v' + \eta_x p \\ \rho v v' + \eta_y p \\ (\rho e + p)v' \end{array} \right\}$$

$$R' = \frac{1}{J} \left\{ \begin{array}{c} 0 \\ \xi_x \tau_{xx} + \xi_y \tau_{xy} \\ \xi_x \tau_{xy} + \xi_y \tau_{yy} \\ \xi_x \beta_x + \xi_y \beta_y \end{array} \right\}, S' = \left\{ \begin{array}{c} 0 \\ \eta_x \tau_{xx} + \eta_y \tau_{xy} \\ \eta_x \tau_{xy} + \eta_y \tau_{yy} \\ \eta_x \beta_x + \eta_y \beta_y \end{array} \right\}$$

$$\beta_x = u\tau_{xx} + v\tau_{xy} + \kappa\frac{\partial T}{\partial x}$$

$$\beta_y = u\tau_{xy} + v\tau_{yy} + \kappa\frac{\partial T}{\partial y}$$

3.3 Iterative Scheme

Considering a single cell in curvilinear coordinates with surface $d\xi d\eta$:

$$\int \frac{dQ'}{dt} d\xi d\eta = \frac{\partial}{\partial t} \int Q' \xi \eta = \frac{\partial}{\partial t} \int \frac{Q}{J} d\xi d\eta$$

and:

$$\frac{d\xi d\eta}{J(\xi,\eta/x,y)} = J(x,y/\xi,\eta)d\xi d\eta = \mathcal{A}$$

where $\mathcal{A}$ is the area of the cell. Integrating each flux for cell i,j yields:

$$\int_{\mathcal{A}} \frac{\partial E'}{\partial \xi} d\xi d\eta = (E'_{i+1/2} - E'_{i-1/2})d\eta$$

$$\int_{\mathcal{A}} \frac{\partial F'}{\partial \eta} d\xi d\eta = (F'_{j+1/2} - F'_{j-1/2})d\xi$$

$$\int_{\mathcal{A}} \frac{\partial R'}{\partial \xi} d\xi d\eta = (R'_{i+1/2} - R'_{i-1/2})d\eta$$

$$\int_{\mathcal{A}} \frac{\partial S'}{\partial \eta} d\xi d\eta = (S'_{j+1/2} - S'_{j-1/2})d\xi$$

Defining:

$$\vec{l'} = \frac{\vec{\nabla}\xi}{J} d\eta, \ \vec{m'} = \frac{\vec{\nabla}\eta}{J} d\xi, \ U = u'\frac{d\eta}{J} = \vec{v} \cdot \vec{l'}, \ V = v'\frac{d\xi}{J} = \vec{v} \cdot \vec{m'}$$

where $\vec{l'}$ is normal to ξ-face with magnitude equal to the element surface area and pointing in direction of increasing η and $\vec{m'}$ is normal to η-face with magnitude equal to the element surface area and pointing in direction of increasing ξ. Assuming $d\xi = d\eta = 1$, without loss of generality, and redefining the symbols $E, F, R,$ and S yields:

$$\frac{d}{dt}(Q_{ij}\mathcal{A}_{ij}) + (E_{i+1/2} - E_{i-1/2}) + (F_{j+1/2} - F_{j-1/2}) =$$
$$(R_{i+1/2} - R_{i-1/2}) + (S_{j+1/2} - S_{j-1/2})$$

$$E = \left\{ \begin{array}{c} \rho U \\ \rho u U + l'_x p \\ \rho v U + l'_y p \\ (\rho e + p) U \end{array} \right\}, F = \left\{ \begin{array}{c} \rho V \\ \rho u V + m'_x p \\ \rho v V + m'_y p \\ (\rho e + p) V \end{array} \right\}$$

$$R = \left\{ \begin{array}{c} 0 \\ l'_x \tau_{xx} + l'_y \tau_{xy} \\ l'_x \tau_{xy} + l'_y \tau_{yy} \\ l'_x \beta_x + l'_y \beta_y \end{array} \right\}, S = \left\{ \begin{array}{c} 0 \\ m'_x \tau_{xx} + m'_y \tau_{xy} \\ m'_x \tau_{xy} + m'_y \tau_{yy} \\ m'_x \beta_x + m'_y \beta_y \end{array} \right\}$$

$$\beta_x = u\tau_{xx} + v\tau_{xy} + \kappa \frac{\partial T}{\partial x}$$

$$\beta_y = u\tau_{xy} + v\tau_{yy} + \kappa \frac{\partial T}{\partial y}$$

$$\tau_{xx} = 2\mu \frac{\partial u}{\partial x} + (\mu_v - \frac{2}{3}\mu)(\frac{\partial u}{\partial x} + \frac{\partial v}{\partial y}), \tau_{yy} = 2\mu \frac{\partial v}{\partial y} + (\mu_v - \frac{2}{3}\mu)(\frac{\partial u}{\partial x} + \frac{\partial v}{\partial y}), \tau_{xy} = \mu(\frac{\partial u}{\partial y} + \frac{\partial v}{\partial x})$$

By Sutherland's law (T_∞ and μ_∞ are free stream temperature and free stream dynamic viscosity, S is Sutherland's constant, and T is calculated temperature):

$$\frac{\mu}{\mu_\infty} = (\frac{T}{T_\infty})^{3/2} \frac{T_\infty + S}{T + S}$$

Calculating thermal conductivity (where Pr is Prandtl number, γ is ratio of specific heat, and M_∞ is the freestream Mach number) becomes:

$$\kappa = \frac{\mu}{(\gamma - 1)M_\infty{}^2 Pr}$$

3.4 Van Leer's Flux Vector Splitting

There are many algorithms to solve the above equations, but Van Leer flux vector splitting with reconstruction method of third order upwind modified essentially non-oscillatory (ENO) limiter ($\kappa = 0.3333$) was chosen because it converged faster in the inviscid case simulation, compared to Roe, AUSM+ and Modified Roe. Flux vector splitting implies for a given flux $\mathcal{F}$, it is separated into two segments [15]:

$$\mathcal{F} = \mathcal{F}^+ + \mathcal{F}^-$$

where all eigenvalues of $\partial \mathcal{F}^+/\partial \mathcal{Q}$ are positive and all eigenvalues of $\partial \mathcal{F}^-/\partial \mathcal{Q}$ are negative. Consider the flux in the x-direction for simplicity, the Van Leer flux vector splitting for a nominal flux $\mathcal{F}$ (with Mach number M, speed of sound a, pressure p, density ρ, velocity $\vec{v}$, ration of specific heats γ, and enthalpy per unit mass h_0) becomes [16]:

$$\mathcal{F} = \left\{ \begin{array}{c} \rho u \\ \rho u u + p \\ \rho u v \\ (\rho e + p)u \end{array} \right\} \Rightarrow \mathcal{F}^\pm = \pm \frac{\rho a (M \pm 1)^2}{4} \left\{ \begin{array}{c} 1 \\ u \pm \frac{a}{\gamma}(-M \pm 2) \\ v \pm \frac{a}{\gamma}(M \pm 2) \\ h_0 - \frac{a^2(-M \pm 1)^2}{\gamma + 1} \end{array} \right\}$$

flux value becomes:

$$\mathcal{F} = \left\{ \begin{array}{ll} \mathcal{F}^- & M < -1 \\ \mathcal{F}^- + \mathcal{F}^+ & -1 < M < 1 \\ \mathcal{F}^+ & M > 1 \end{array} \right.$$

Most heat flux is contribute in the wall normal direction, however *GASPex* also calculates cross cells for flux. Details on *GASPex* technical methods are available in reference [16].

3.5   Modified ENO Reconstruction

The Modified Essentially Non-Oscillatory (ENO) limiter achieves uniform accuracy and controls local oscillation via a non-linear stencil selection. If forward and backward gradients change in sign, the reconstruction reduces to a first order reconstruction [16]. The ENO reconstruction method is stable and accurate [12]. It builds high-order reconstruction by choosing the minimum of two differences to the n-order interpolation. The selection of $\kappa = 0.3333$ creates a third-order accurate reconstruction.

One-dimensional reconstruction $Q(x)$ of one-dimensional function $\mathcal{Q}(x)$ is $Q(x) = \mathcal{Q}(x) + \mathcal{O}(\Delta x^3)$, which has conditions [15]:

1- $\mathcal{Q}(x)$ is a smooth function,

2- $Q_i = \int_{x_{i-1/2}}^{x_{i+1/2}} Q_i(x) dx$,

3- Total value, TV, which is: $TV(Q) = \int_{x_{i-1/2}}^{x_{i+1/2}} |\frac{dQ}{dx}| dx$, holds: $TV(Q_i(x)) \le TV(\mathcal{Q}(x)) + \mathcal{O}(\Delta x^3)$.

$Q(x)$ becomes [15]:

$$Q_i(x) = Q_i - \frac{\Delta Q_{i-a+3/2} - \Delta Q_{i-a+1/2}}{24} + \frac{1}{\Delta x}[\Delta Q_{i-a+1/2} + (a - \frac{1}{2})[\Delta Q_{i-a+3/2} - \Delta Q_{i-a+1/2}] \times$$

$$(x - x_i) + \frac{\Delta Q_{i-a+3/2} - \Delta Q_{i-a+1/2}}{2(\Delta x)^2} \times (x - x_i)^2$$

where $\Delta Q_{i+1/2} = Q_{i+1} - Q_i$ and a is:

$$a = \begin{cases} 0 & if \quad |\Delta Q_{i+1/2}| \le |\Delta Q_{i-1/2}| \quad and \quad |\Delta Q_{i+3/2} - \Delta Q_{i+1/2}| \le |\Delta Q_{i+1/2} - \Delta Q_{i-1/2}| \\ 1 & if \quad |\Delta Q_{i+1/2}| \le |\Delta Q_{i-1/2}| \quad and \quad |\Delta Q_{i+3/2} - \Delta Q_{i+1/2}| > |\Delta Q_{i+1/2} - \Delta Q_{i-1/2}| \\ 1 & if \quad |\Delta Q_{i+1/2}| > |\Delta Q_{i-1/2}| \quad and \quad |\Delta Q_{i+1/2} - \Delta Q_{i-1/2}| \le |\Delta Q_{i-1/2} - \Delta Q_{i-3/2}| \\ 2 & if \quad |\Delta Q_{i+1/2}| > |\Delta Q_{i-1/2}| \quad and \quad |\Delta Q_{i+1/2} - \Delta Q_{i-1/2}| > |\Delta Q_{i-1/2} - \Delta Q_{i-3/2}| \end{cases}$$

Chapter 4

Method of Solution

The commercial software ANSYS ICEM CFD was used to generate the computational domain. The grid was generated in the CGNS format. All the lengths on the computational domain were a 1:1 scale to the actual geometry (physical model). This scaling helps prevention of confusion in unit conversion. All calculations and variable units follow the metric system.

The flow solver was the commercial software *GASPex*. This is the export controlled (one without real gas models used for thermo-chemical reactions) version of the commercial software *GASP*.

4.1   Grid Structure

A multi-block model was generated using the commercial code ICEM CFD, with three main sections: Inflow Zone, Object Zone, and Lower Tip Zone. The purpose of the Inflow Zone is to create a space between the inlet boundary and the object or shock wave in which no disturbance is propagated upstream and hence it is not sensed by the inflow boundary. In models with a sharp tip, the flow disturbance propagates upstream into one or two cells. In order to eliminate this propagation, the Lower Tip Zone was generated under the tip so that flow passes through that face and resolves this issue. The Inflow Zone is divided into two regions: Zone 1 from inlet boundary to the lower tip and Zone 3 from the inlet boundary to the tip of the sharp edge. The Object Zone is divided into three zones: Zone 4 captures the forward wedge, Zone 5 captures the aft wedge and Zone 6 is the flat top of the object. Fig. 4.1 denotes the geometry partitions. Mesh orthogonality near the wall is important to achieve an accurate calculation of surface heat transfer. Dividing the object zone into three sub-zones forces ICEM CFD

Table 4.1: Grid cells per zone

Zone	Coarse	Mid	Fine
1	20×20	40×40	80×80
2	20×20	40×40	80×80
3	20×700	40×1400	80×2800
4	650×700	1300×1400	2600×2800
5	320×700	640×1400	1280×2800
6	500×700	1000×1400	2000×2800
Total	1,043,000	4,175,200	16,700,800

to generate a nearly orthogonal mesh on each wedge. The number of cells in each zone for each mesh is shown in Table 4.1.

A total of three separate grids were utilized for the grid refinement study. Each successive grid was obtained from the previous grid by doubling the number of cells in each direction for every region.

Zones 1 to 3 (upstream of the first shock wave): The grid spacing in the x-direction is uniform. The coarse grid utilized 20 cells with spacing $\Delta s/L_p \simeq 0.0085$ (where Δs is grid spacing along the lower surface). The grid spacing for zones 1 and 2 in the y-direction is also $\Delta n/L_p \simeq 0.0085$ (Δn is grid spacing perpendicular to the lower surface).

Zone 4 (downstream of first shock wave, and over the forward wedge): This region has 650 cells in the x-direction with the first grid cell having $\Delta s/L_f \simeq 0.0015$. The grid spacing in the y-direction is as same as zone 3 for all zones downstream of the first shock wave, which contains 600 cells and the first $\Delta n/H_t \simeq 0.00148$. The domain height should be able to capture the bow shock exiting a plane parallel to inflow, thus after the initial simulation we noted that $4H_t$ height (144 mm) prevents the oblique shock from exiting through top boundary (the boundary parallel to the object). This
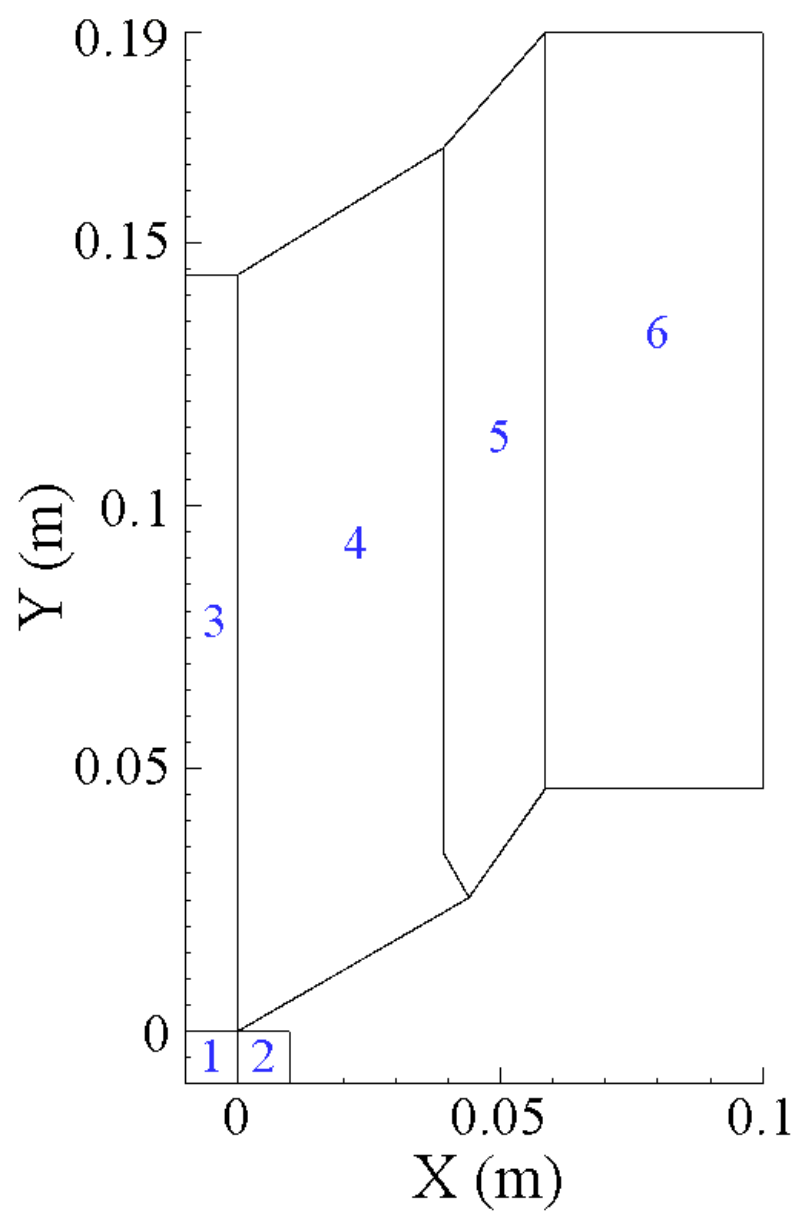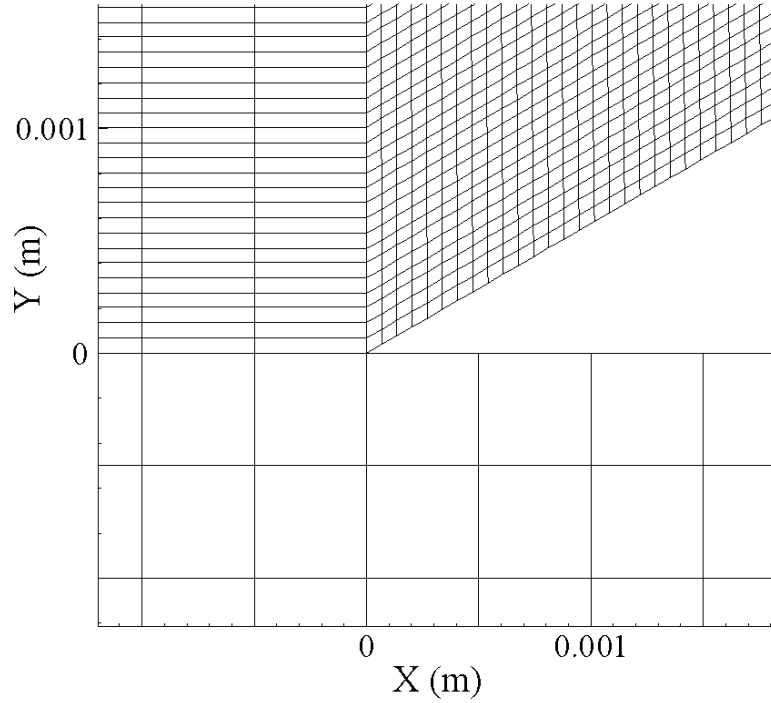
Figure 4.1: Mesh Zones

Figure 4.2: Mesh Around Object Tip

height is kept constant in the model (except where we have lower tip zones), and as a result the top boundary is always parallel to the object. The calculated boundary layer thickness using Wilcox's Eddybl program [13] and Hoffmann *et al.* [14] at $x = L_f$ (with the assumption of no aft wedge) is $\delta = 1.135$ mm. In the direction away from the surface, the coarse grid contains 15 cells, the mid grid contains 30 cells, and the fine grid contains 60 cells within the boundary layer. The grid size expands in the y-direction and for the last grid cell $\Delta n / H_t \simeq 0.00438$.

Zone 5 (downstream of first shock wave, and over the aft wedge): This region contains 320 cells. In this case, $\Delta s / L_a \simeq 0.0031$.

Zone 6 (flat section at the end of the object): This region has 500 cells equally distributed. Fig. 4.2 illustrates the mesh spacing around the tip, and Fig. 4.3 shows near orthogonal cells near the lower surface.
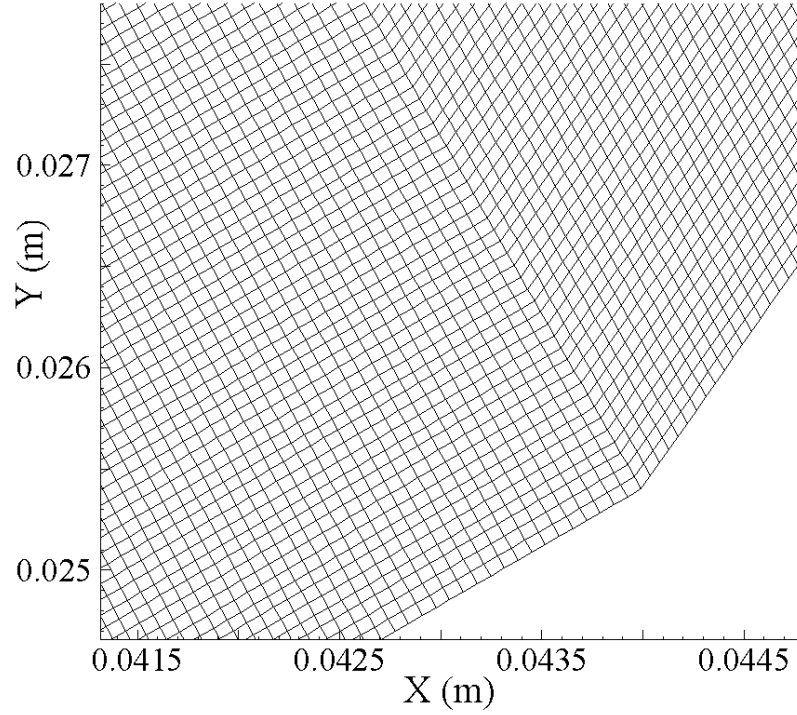
Figure 4.3: Near Orthogonal Cells

4.2 Boundary Condition

The inflow used `fixed at Q` boundary condition (*i.e.* values are set according to `Q`
`source` input). `Q source` is set to values according to Table 2.2 for each case. Other
boundaries (outflow and farfield) except the double wedge surface are first order extrap-
olation. The computational domain is initialized to have the same value as `Q source`.
This corresponds to an impulsive start of the wind tunnel. These are the general settings
for all inviscid and laminar cases.

In the inviscid case, the double wedge has boundary type `tangency` and the simula-
tion is continued to reach steady state (normalized residual less than 10^{-3} or absolute
residual less than 10^{-12}). The time step is selected based on CFL=1 based on `Q`
`infinity` and an automatic time step limiter was added to prevent changes more than
one percent by using a five percent restoration factor.

For laminar cases, the double wedge boundary type is `NoSlipT=Tw` and a second

order accurate dual time stepping with physical time step 10^{-7} s and pseudo time step 10^{-8} s. A maximum of 20 inner iterations are performed if the convergence criteria are not met (normalized residual less than 10^{-2} or absolute residual less than 10^{-8}). The solution is saved for every 0.01 ms for all time dependent cases, and is also saved at the time where Swantek and Austin [2] report the flow has reached steady state. Time dependent cases are set to run up to 4.0 ms, but will stop simulation if it reaches steady state before that. The flow reaches steady state when the surface heat transfer values change less than 1%. In particular, the location of the drop in heat transfer on the forward wedge, and magnitude of the maximum heat transfer on the aft wedge are closely related to the boundary layer separation and hence are sensitive indicators of convergence to steady state.

4.3   Hardware Usage

A total of three high performance computer clusters (HPC) were used for this research, two from Rutgers University's Center for Computational Design (CCD) and one from Rutgers University's School of Engineering (SOE). CCD's clusters are called Prigogine and Tupolev. Their specifications are listed in Table 4.2. The 8 MJ Fine mesh case ran a total amount of 16 days to finish its computation on the SOE cluster.

Table 4.2: Double wedge configuration

System	Cores Used	Processors	Memory per core
Prigogine	48	2.4 GHz AMD Opteron $^{\text{TM}}$	1 GByte
Tupolev	48	2.4 GHz AMD Opteron $^{\text{TM}}$	1 GByte
SOE	128	3.2 GHz Intel$^\circledR$ Xeon$^\circledR$ E5	8 GByte

Chapter 5

Results

For the inviscid case, the coarse grid was chosen to be investigated in the high enthalpy case. The characteristic time is t=68 μs (*i.e.*, the time required for a fluid element to traverse the computational domain based on the velocity downstream of the forebody shock). Laminar cases were solved using the implicit dual time stepping simulation with data saved at 0.01 ms physical time increments. The values for Mach, pressure, and temperature for the flowfield and surface heat transfer, skin friction, and surface pressure were studied. Surface heat transfer is also compared between experimental results in each case at the physical time reported by the experiment, and with numerical values at steady state.

5.1 Inviscid Case

The inviscid case has two segments: the region immediate after the shock (forebody), which is used to compare with analytical values from [10], and the flow over the double wedge region, which is studied to understand flow structure after SWBLI.

5.1.1 Forebody

Table 5.1 shows the analytical [10] and computed (coarse grid) values for the shock angle (β), Mach number, pressure ratio and temperature ratio for the region immediate after the forebody shock. The computed results are in excellent agreement with the theory. Mach contours and flow segments are shown in Fig. 5.1.

Table 5.1: Inviscid weak forebody shock values

Variable	Theory	Numerical	Error %
β	$39.75°$	$39.74°$	0.25
M	2.49	2.51	0.90
P/P_∞	24.15	24.146	0.02
T/T_∞	4.99	4.98	0.09

5.1.2 Aft Wedge

As shown in Fig. 5.2, the flow approaches the forward wedge and creates an oblique shock at location 1. By the value of downstream Mach number, it can be seen that this oblique shock is the weak shock solution, while location 2 indicates a strong oblique shock. Location 3 is inside the subsonic region, and location 4 is the interaction point between weak shock, strong shock and slip line. After the flow is affected by the forward wedge, it changes velocity direction to become parallel to the lower surface. A shock wave is reflected at location 5 from the wall impacting the slip line at location 6. An expansion wave forms toward the surface and creates another shock reflection at location 7, at the double wedge intersection. Location 8 is a subsonic region which has an expansion fan on its immediate left. Location 9 is on the top of the double wedge and as expected, an expansion fan is formed at that point.

5.2 Laminar Low Enthalpy Case

For the low enthalpy case, the coarse and mid grids were used for the simulation. Both cases were simulated to a corresponding flow time of 4.0 ms.

5.2.1 Coarse Grid

Convergence to steady state of the low enthalpy case with the coarse grid was investigated. Fig. 5.3 shows surface heat transfer for this grid. Fig. 5.4 and Fig. 5.5 show values for pressure and skin friction for same grid. From these figures one could see flow has not reached steady state at t=4.0 ms.
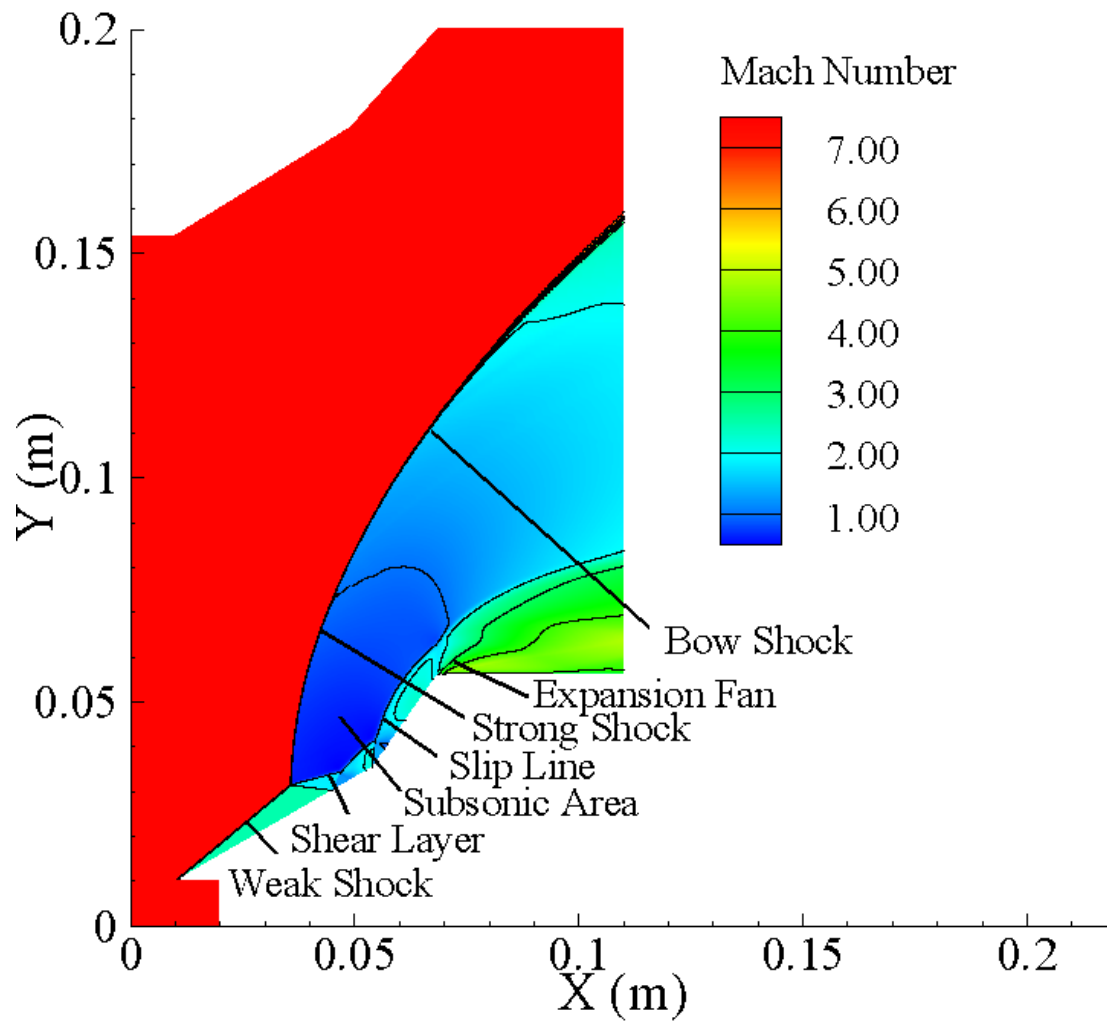
Figure 5.1: Flow Structure (inviscid case)
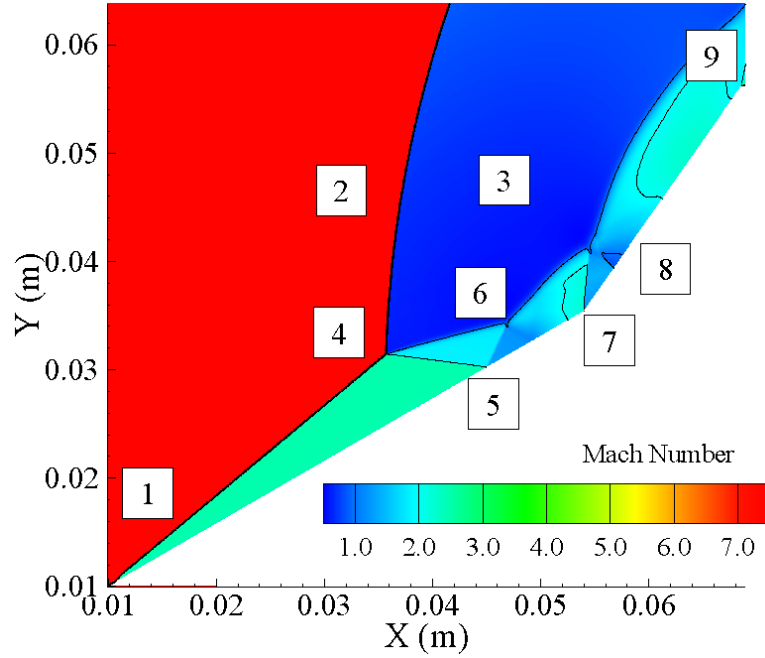
Figure 5.2: Shock Interactions (inviscid case)

5.2.2 Mid Grid

The second case for the low enthalpy configuration used the mid grid, where Fig. 5.6, Fig. 5.7, and Fig. 5.8 show values of surface heat transfer, pressure and skin friction respectively. These figures indicates that flow has reached steady state at t=3.3 ms.

The heat transfer, after an initial rise and fall, decreases gradually until it reaches the separation bubble and has a sudden drop and becomes close to zero. This is the region of the flow where nominally the rotational flow has a much slower speed than other regions. Close to the vicinity of the forward and aft wedge connection, the surface heat transfer reaches its minimum value and gradually increases on the aft wedge. Comparing values from the coarse and the mid grid shows that values of surface heat transfer and skin friction increase as the mesh becomes more dense. Since the coarse grid does not reach steady state, it generates higher values for surface pressure in the same time that the mid grid has reached steady state, and its values are lower than the coarse grid.

Fig. 5.9 and Fig. 5.10 show Mach contours for 3.0 ms and 4.0 ms for the mid grid.
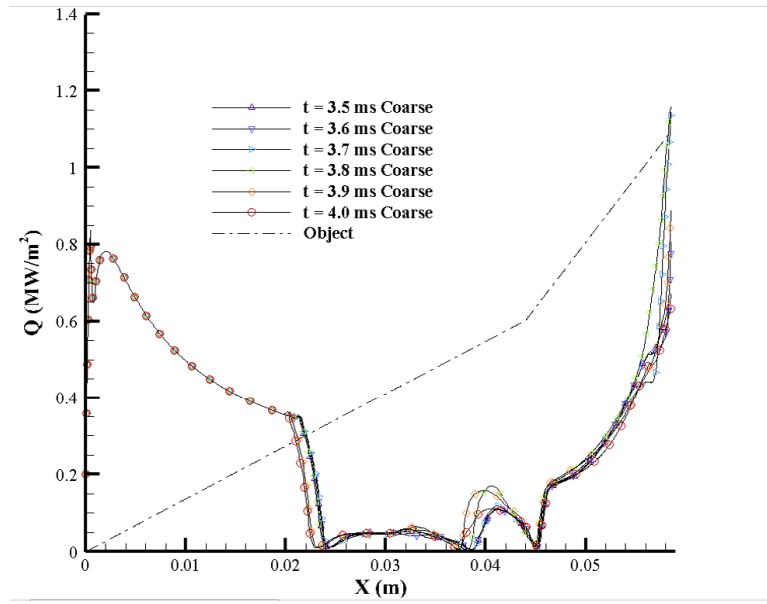
Figure 5.3: Heat Transfer, 2MJ Coarse Grid
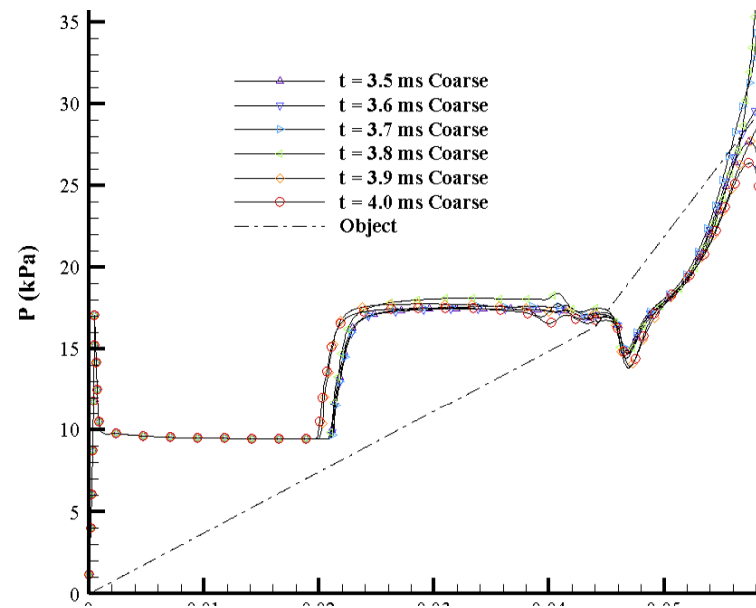
Figure 5.4: Pressure, 2MJ Coarse Grid
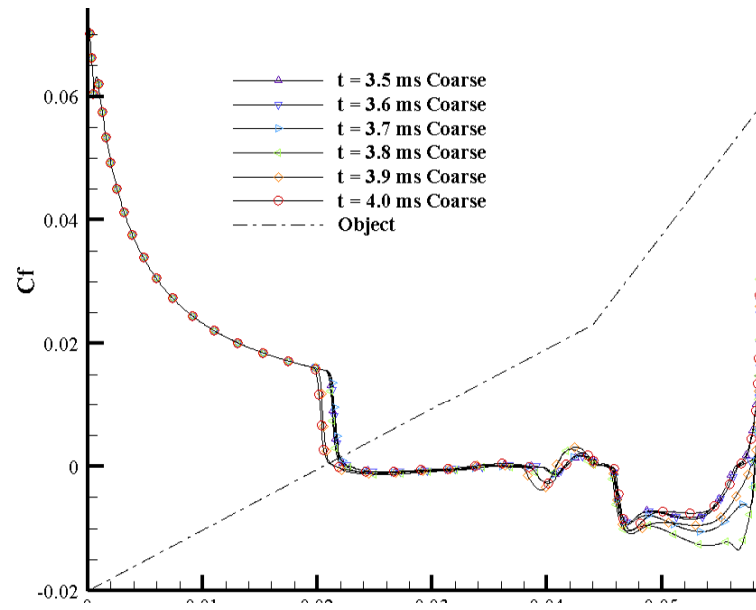
Figure 5.5: Skin Friction, 2MJ Coarse Grid
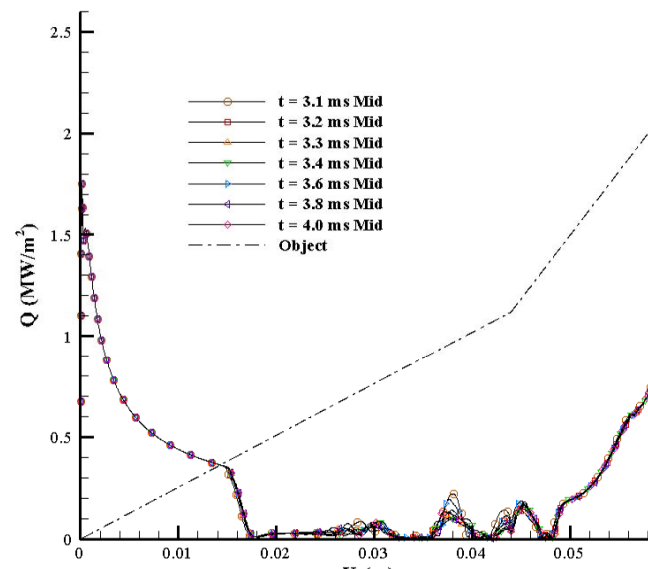
Figure 5.6: Heat Transfer, 2MJ Mid Grid
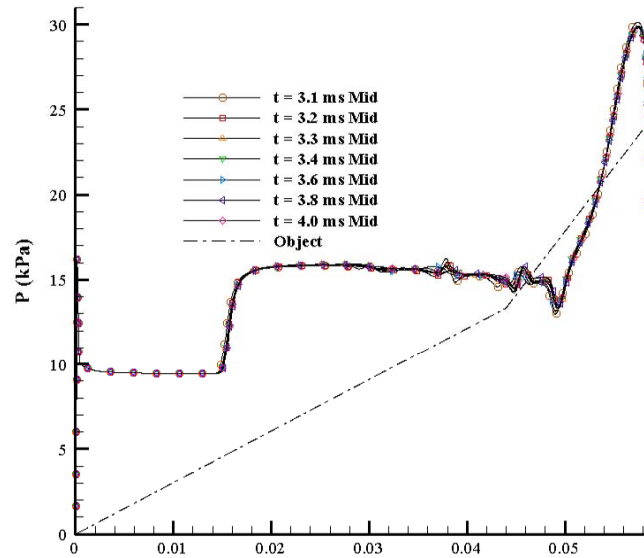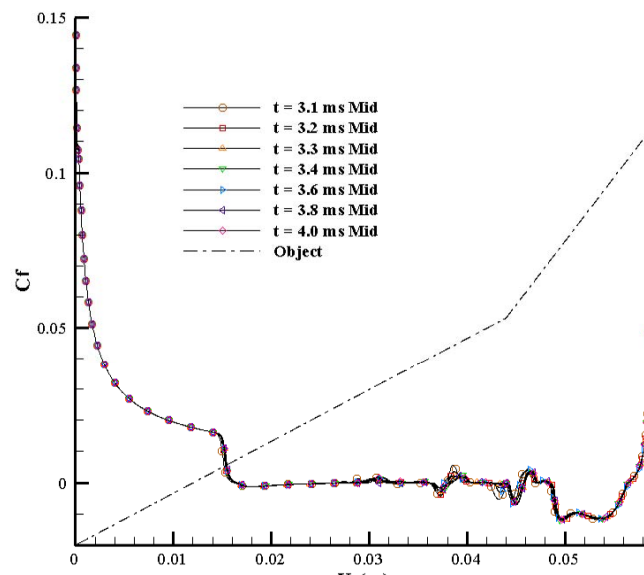
Figure 5.7: Pressure, 2MJ Mid Grid
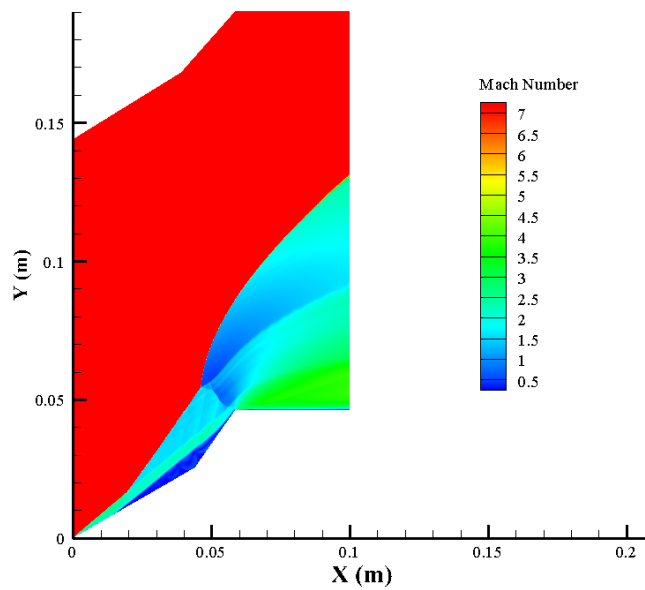

Figure 5.8: Skin Friction, 2MJ Mid Grid
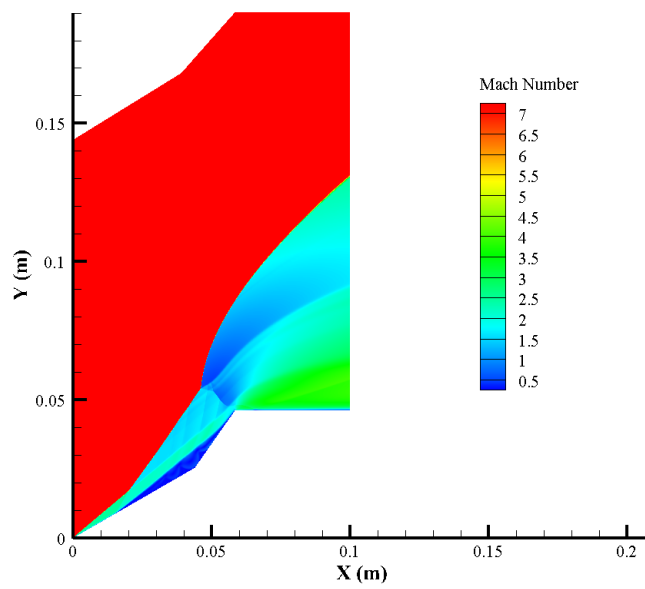
Figure 5.9: Mach contour at t = 3.0 ms, 2MJ Mid Grid
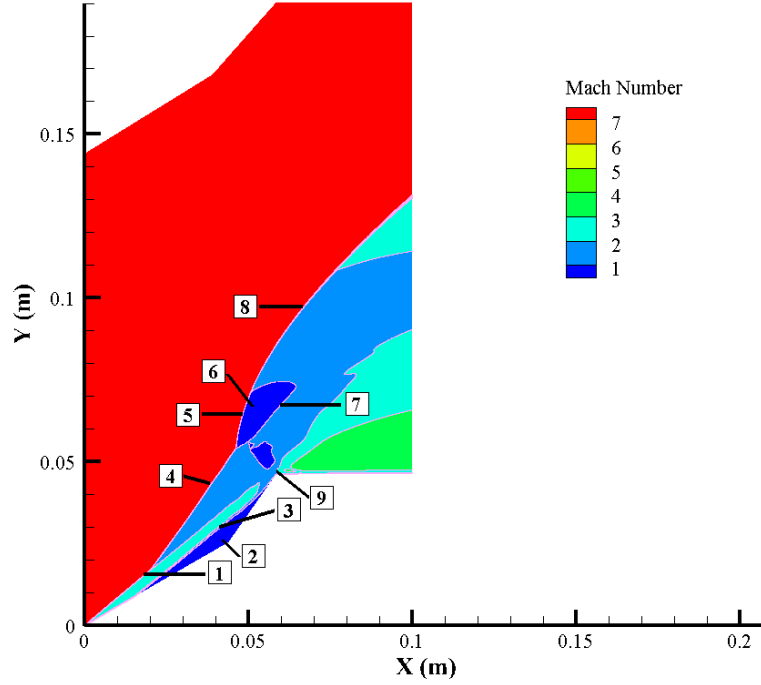

Figure 5.10: Mach contour at t = 4.0 ms, 2MJ Mid Grid

Figure 5.11: Detailed Mach contours configuration at t = 0.372 ms

The flow structure in these cases are similar to the inviscid case; however, with the addition of viscosity, the boundary layer now separates and creates a separation bubble. Referring to Fig. 5.11, location 1 indicates the weak oblique forebody shock. Point 2 denotes the recirculation region between two wedges. The upper boundary of this region (location 3) is a slip line. Supersonic flow over this region is forced to adopt the new velocity direction which acts as a new wedge. The new weak oblique shock is identified with location 4. Location 5 is on the edge of the strong oblique shock wave, and formed between the freestream Mach and section containing location 6. Surrounding location 6 (the subsonic region) is slip line which contains location 7. Location 8 indicates the bow shock and location 9 indicates the expansion fan on top of the model.

5.2.3   Steady State Heat Transfer

According to Swantek and Austin [2] the experimental heat transfer reached steady state at $t = 0.327$ ms. Fig. 5.12 compares values between experiment's reported steady state values and the numerical values at steady state. It is clearly evident that
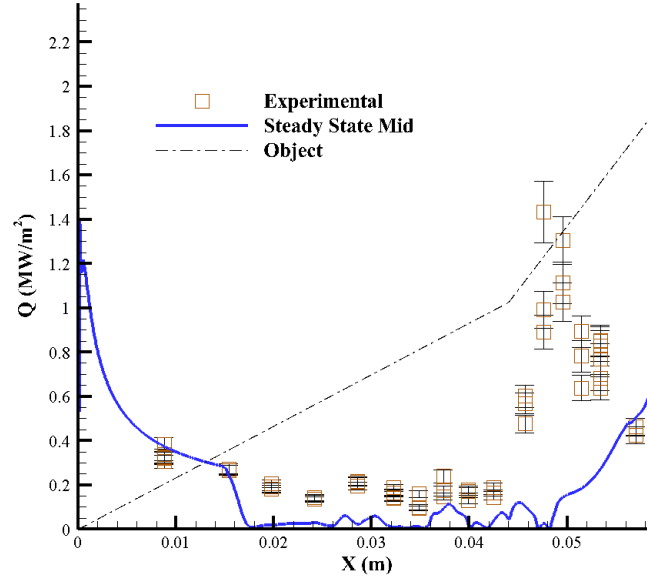
Figure 5.12: Surface heat transfer comparison with experiment at Steady State

the two surface heat transfer profiles don't agree. In another comparison, Fig. 5.13 compares the computed surface heat transfer with experiment, both at $t = 0.327$ ms (reported time where flow reaches steady state in the experiment). The computed and experimental peak heat transfer at reattachment ($x = 47$ mm) show close agreement; however, significant disagreement is evident in the separated flow region (16 mm < x < 44 mm). Comparison of the computed heat transfer profile at $t = 0.327$ ms with the computed steady state heat transfer profile in Fig. 5.12 indicates that the computed flowfield is definitely unsteady at $t = 0.327$ ms.

5.3   Laminar High Enthalpy Case

For the high enthalpy case, the three grid sequences (coarse, mid, and fine) were simulated. Initially, all cases were set to reach 2.0 ms simulation, but as each case reached steady state, it was stopped. Mach contours and flow structure are similar to the low enthalpy case. Due to the change of enthalpy, the surface heat transfer, surface pressure, and skin friction differ from the low enthalpy case.
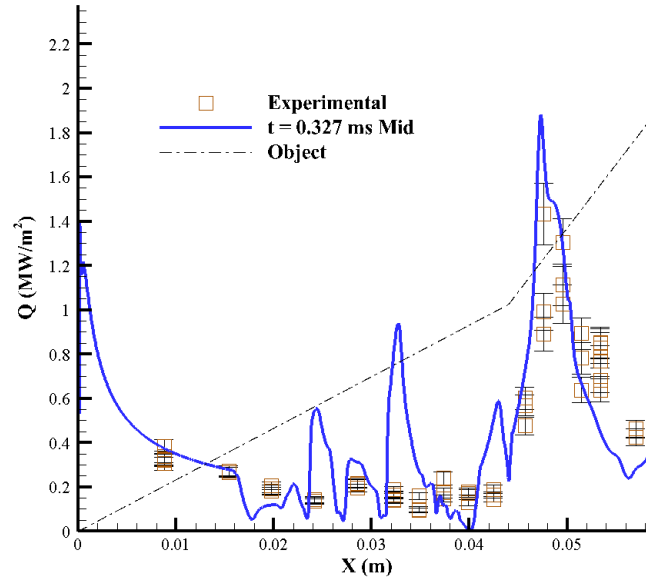
Figure 5.13: Surface heat transfer comparison with experiment at t = 0.372 ms

5.3.1 Coarse Grid

For the coarse grid, surface heat transfer, pressure and skin friction on the double wedge surface are shown in Fig. 5.14, Fig. 5.15, and Fig. 5.16. In this case, flow reaches steady state at 1.8 ms.

5.3.2 Mid Grid

Values of surface heat transfer, pressure, and skin friction for the high enthalpy near steady state are shown in Fig. 5.17, Fig. 5.18, and Fig. 5.19. The flow reaches steady state at 1.2 ms.

5.3.3 Fine Grid

Lastly for the fine grid high enthalpy case, the surface heat transfer is shown Fig. 5.20, pressure is shown in Fig. 5.21, and skin friction is shown Fig. 5.22. In this case, flow reaches steady state at 1.7 ms.
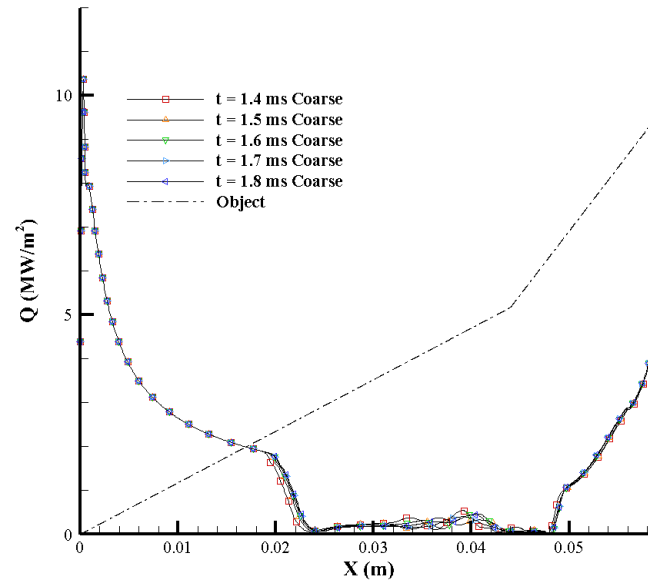
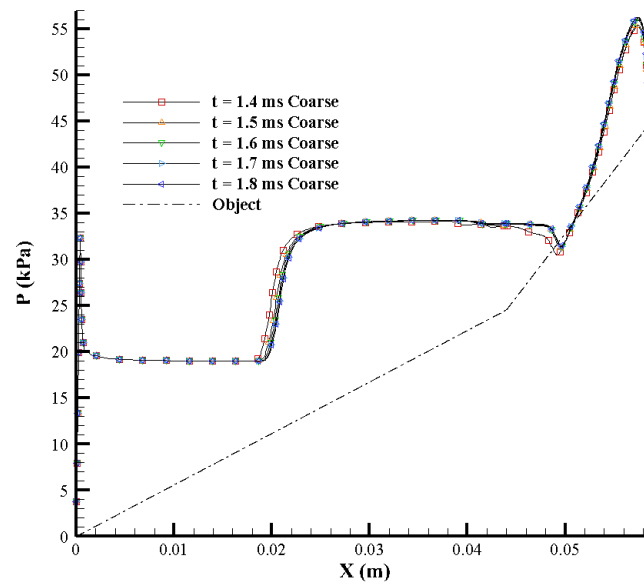Figure 5.14: Heat Transfer, 8MJ Coarse Grid

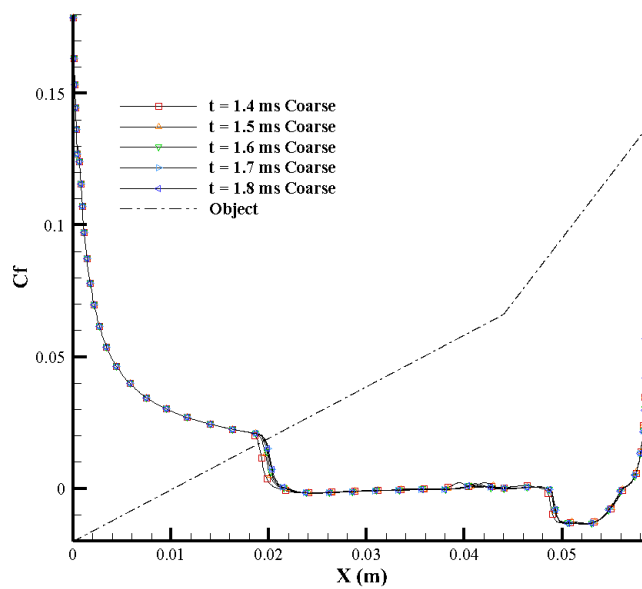Figure 5.15: Pressure, 8MJ Coarse Grid
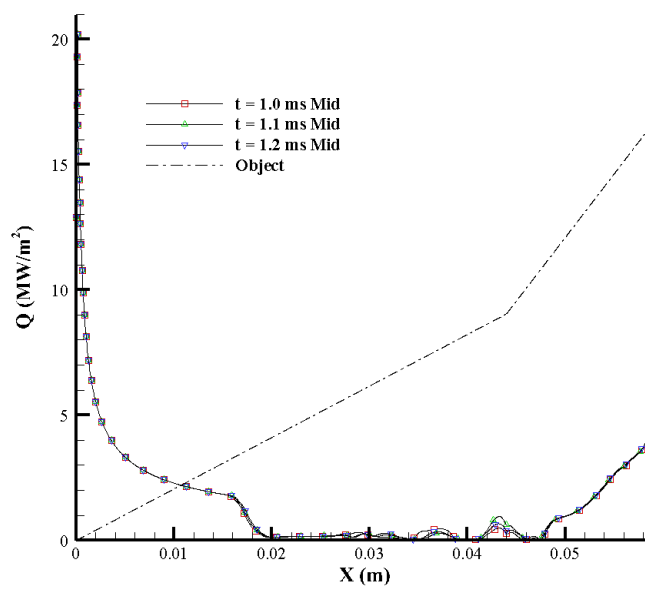
Figure 5.16: Skin Friction, 8MJ Coarse Grid

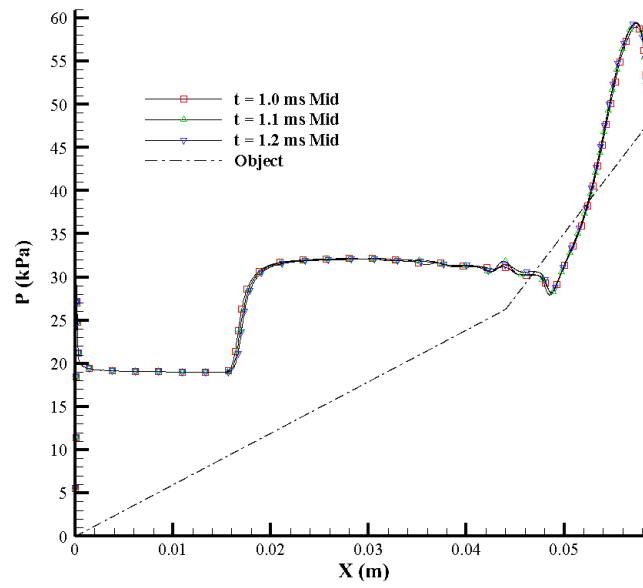Figure 5.17: Heat Transfer, 8MJ Mid Grid
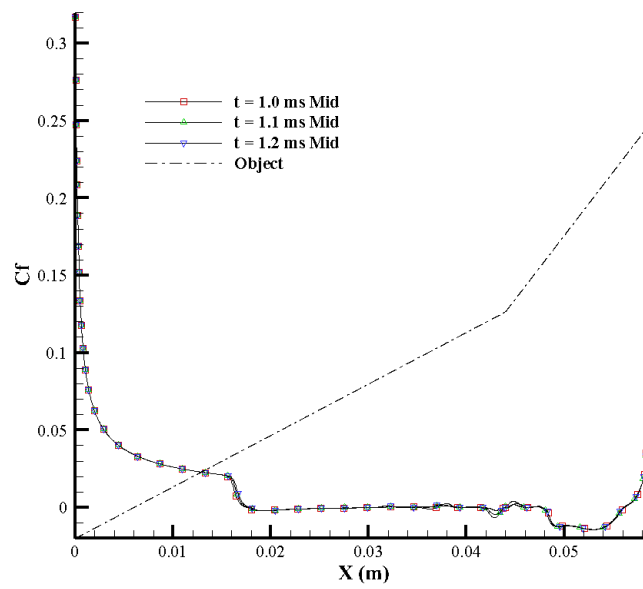
Figure 5.18: Pressure, 8MJ Mid Grid

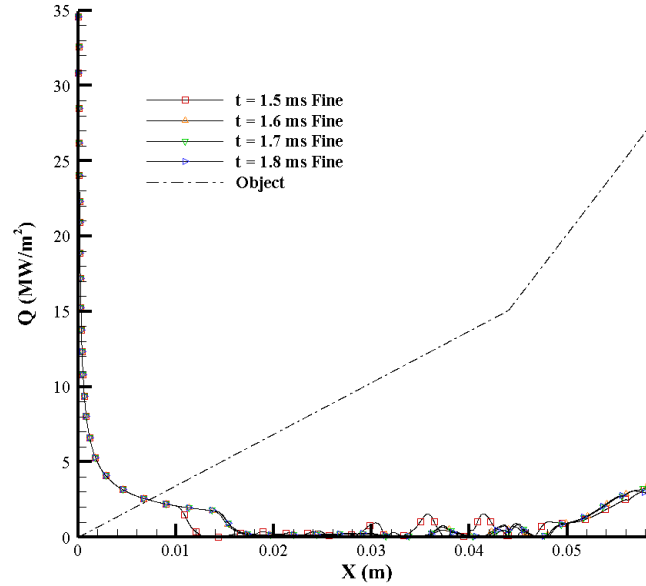Figure 5.19: Skin Friction, 8MJ Mid Grid

Figure 5.20: Heat Transfer, 8MJ Fine Grid

A noticeable difference between these three cases is that the time required for the flow to reach steady state varies between the three cases. Another major difference is the bubble size which grows as the mesh becomes more dense. In the high enthalpy case, the maximum value for surface heat transfer, pressure, and skin friction increases as mesh becomes more dense. This was also observed in low enthalpy cases.

Fig. 5.23 compares the surface heat transfer between grid sequences and shows that prior to the shock interaction on the forward wedge, the surface heat transfer is approximately 1.7 MW/m^2. On the aft wedge, where there is an increase in surface heat transfer value, all three grid sequences reach the same value.

5.3.4 Steady State Heat Transfer

The steady state heat transfer values from the experiment and computation are compared in Fig. 5.24. As seen in the low enthalpy case, the numeric values and experimental heat transfer do not agree.

Fig. 5.25 compares the computed and experimental surface heat transfer at the time
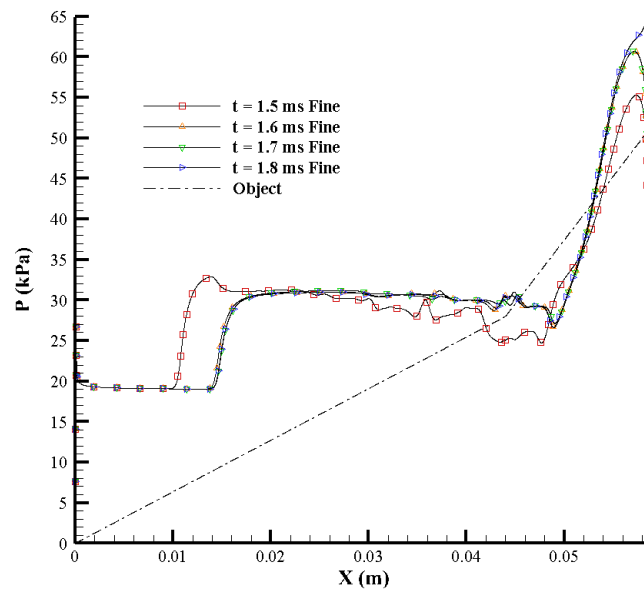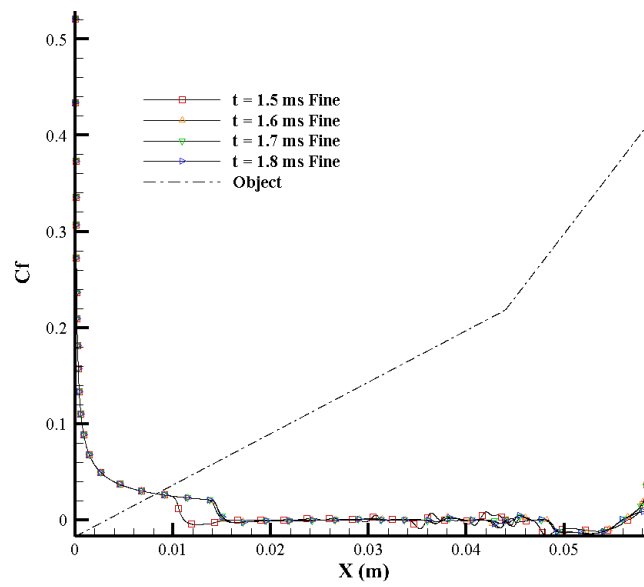
Figure 5.21: Pressure, 8MJ Fine Grid

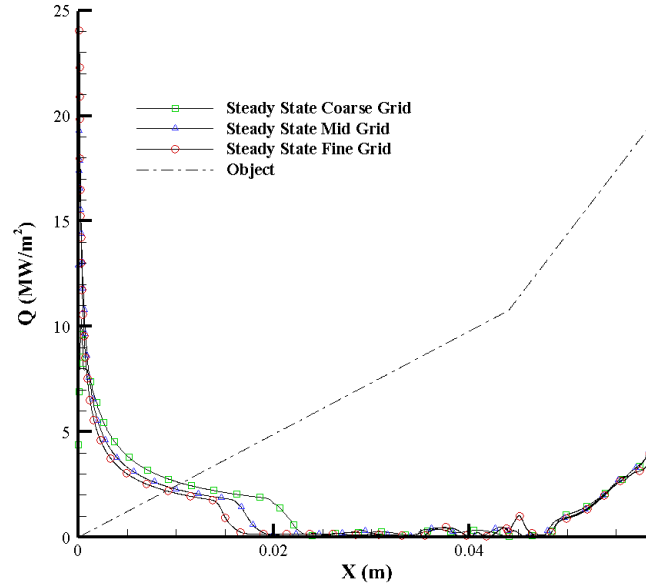Figure 5.22: Skin Friction, 8MJ Fine Grid

Figure 5.23: Heat Transfer, 8MJ Numerical steady state

Swantek and Austin [2] report that flow has reached steady state (0.242 ms). While the location of the maximum heat transfer agrees closely between the computation (fine grid) and experiment, there is significant disagreement in the computed and experimental heat transfer distribution in the separated region. Comparison of the computed heat transfer at $t = 0.242$ ms with the steady state heat transfer profile in Fig. 5.24 indicates that the computed flowfield is definitely unsteady at $t = 0.242$ ms.
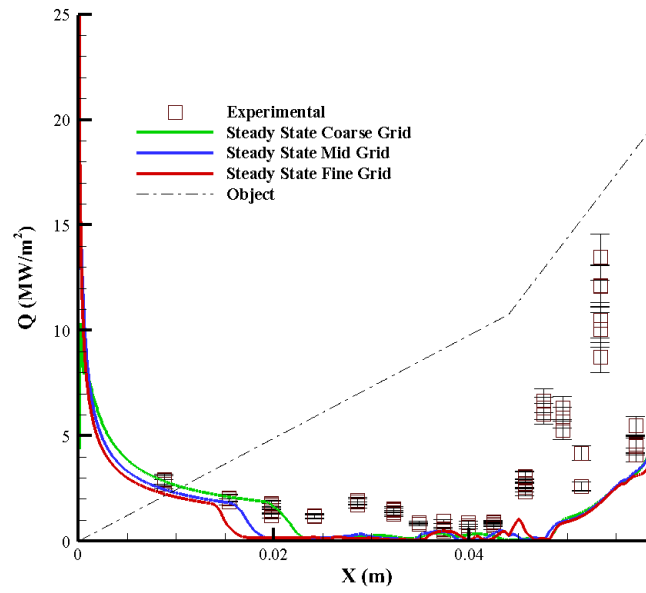
Figure 5.24: Heat Transfer comparison between experiment and numeric in Steady State, 8MJ
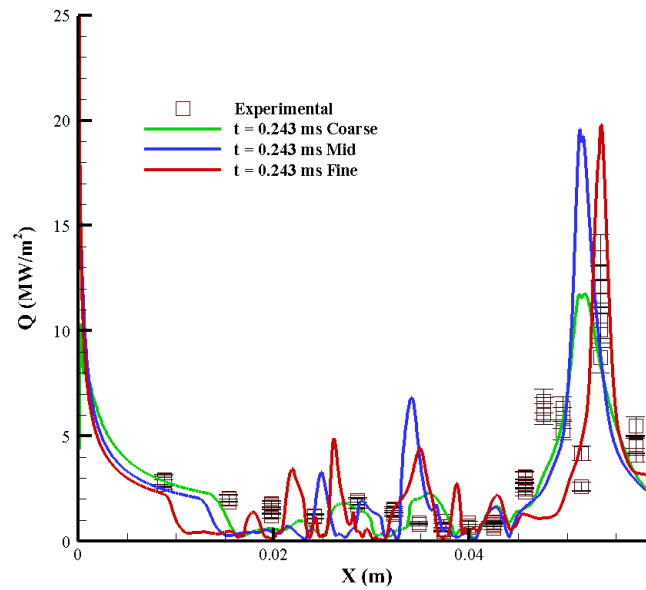

Figure 5.25: Heat Transfer comparison between experiment and numeric in time accurate, 8MJ

Chapter 6

Conclusion

Hypersonic flow past a double wedge at Mach 7.11 and Mach 7.14 for stagnation enthalpies of 2 MJ/kg and 8 MJ/kg, respectively, were simulated. Both cases were simulated for viscous laminar flow, while the Mach 7.14 was also simulated assuming inviscid flow. Field values such as pressure, temperature and Mach number downstream of the forebody shock were compared between theoretical and numerical solution for inviscid Mach 7.14 flow. The computed results for the inviscid flow agree closely with theory. For viscous laminar flow, the surface heat transfer was compared between experiment and computation for three grid sequences. All viscous laminar cases indicate a time to converge to steady state that is much greater than the duration of the experiment. Consequently, the experiments do not appear to have achieved steady flow. For the Mach 7.11 (low enthalpy) case, the coarse grid did not reach steady state after 4.0 ms, while mid grid reached steady state after 3.3 ms. For the Mach 7.14 (high enthalpy) case, the coarse, mid, and fine grids reached steady state at 1.8, 1.2, and 1.7 ms. The experimental "steady state" heat transfer profiles differ significantly from the computed steady state profile for the low and high enthalpy case. The low and high enthalpy simulations do manage to accurately capture peak heat transfer location and magnitude at the time reported by the experiment.

6.1 Comparison with the Experiment

The results of the simulations clearly indicate that the experiment flow fields for the 2 MJ/kg and 8 MJ/kg do not reach steady state. There are three fundamental assumptions of the simulations which may have an effect on this result.

- Perfect gas

The assumption of perfect gas (equilibrium flow) is most certainly accurate for the 2 MJ/kg case, but requires further investigation for the 8 MJ/kg case.

- Impulsive start

  The initial condition for the simulation is the imposition of the freestream conditions at all grid cells. This is not identical to the startup process in the wind tunnel.

- Wall and Three-Dimensional Effect

  The experiment takes place on a three-dimensional object and the numerical simulation assumed (as suggested by the experiment) that flow is two-dimensional. Recent results subsequent to this research by Komives *et al.* [18], and Tumuklu *et al.* [19] indication that the experimental flow field is fully three-dimensional.

Bibliography

[1] Knight, D., Longo, J., Drikakis, D., Gaitonde, D., Lani, A., Nompelis, I., Reimann, B., and Walpot, L., "Assessment of CFD Capability for Prediction of Hypersonic Shock Interactions," *Progress in Aerospace Sciences*, Vol. 48-49, 2012, pp. 8-26.

[2] Swantek, A.B., and Austin, J.M., "Heat Transfer on a Double Wedge Geometry in Hypervelocity Air and Nitrogen Flows," *Proceedings of the 50th AIAA Aerospace Sciences Meeting*, AIAA-2012-0284, Nashville, TN, 2012.

[3] Babinsky, H., Harvey, J.K., *Shock Wave-Boundary-Layer Interactions*. Cambridge Aerospace Series, Cambridge, UK: Cambridge Aerospace Series, 2014.

[4] Dolling, D.S., "Fifty Years of Shock-Wave/Boundary-Layer Interaction Research: What Next?" AIAA Journal, Vol. 39, No. 8 (2001), pp. 1517-1531

[5] Salin, A., Yao, Y., and Zheltovodov, A.A., "Comparison and Improvement of Wall Heat Transfer Prediction in Crossing-Shock-Wave/Turbulent-Boundary-Layer Interaction Conditions," *Proceedings of the 51st AIAA Aerospace Sciences Meeting*, AIAA-2013-0666, Dallas/Ft. Worth Region, TX, 2013.

[6] Borovoy, V.Y., Egorov, I.V., Skuratov, A.S. and Struminskaya. I.V., "Two-Dimensional Shock-Wave/Boundary-Layer Interaction in the Presence of Entropy Layer." AIAA Journal 51.1 (2013): 80-93.

[7] Rouhi Youssefi, M., and Knight, D.D., "Assessment of CFD Capability for High Enthalpy Non-Equilibrium Flows with Strong Viscous-Inviscid Interaction," *Proceedings of the 53rd AIAA Aerospace Sciences Meeting*, AIAA-2015-0580, Kissimmee, FL, 2015.

[8] Patil, V.N., Levin, D.A., Gimelshein, S.G., and Austin, J.M., "Study of shock-shock interactions for the HET facility double wedge configuration using the DSMC approach," *Proceedings of the 43rd Fluid Dynamics Conference*, AIAA-2013-3202, San Diego, CA, 2013.

[9] Private communication, Dr. Joanna Austin, Department of Aerospace Engineering, University of Illinois at Urbana, October 12, 2012.

[10] Ames Research Staff. *Report 1135 Equations, Tables, and Charts for Compressible Flow*. Moffet Field: National Advisory Committee for Aeronautics. 1953. Web. 15 Oct. 2012.

[11] Kundu, P.K., Cohen, I.M., and Dowling, D.R., *Fluid Mechanics*. 4th ed. Waltham, MA: Academic, 2012.

[12] Fjordholm, U.S., Mishra, S., and Tadmor, E., "ENO Reconstruction and ENO Interpolation Are Stable," *Foundations of Computational Mathematics*, Vol. 13, No. 2 (2013): 139-159.

[13] Wilcox, D.C., *Turbulence Modeling for CFD*. 3rd ed. La Canãda, CA: DCW Industries, 2006.

[14] Hoffmann, K.A., Chiang, S., Siddiqui, S., and Papadakis, M., *Fundamental Equations of Fluid Mechanics*. Wichita, KS: Engineering Education Systems, 1996.

[15] Knight, D.D., *Elements of Numerical Methods for Compressible Flows*. Cambridge Aerospace Series, Cambridge, UK: Cambridge Aerospace Series, 2006.

[16] AeroSoft, Inc. *gaspex_userguide*. Blacksburg: AeroSoft, Inc., 2009. Web. 15 Oct. 2012.

[17] Badr, M.A., and Knight, D.D., "Shock Wave Laminar Boundary Layer Interaction Over a Double Wedge in a High Mach Number Flow," *Proceedings of the 52nd AIAA Aerospace Sciences Meeting*, AIAA-2014-1136, National Harbor, MD, 2014.

[18] Komives, J.R., Nompelis, I., and Candler, G.V., "Numerical investigation of unsteady heat transfer on a double wedge geometry in hypervelocity flows," *Proceedings of the 44th AIAA Fluid Dynamics Conference*, AIAA-2014-2354, Atlanta, GA, 2014.

[19] Tumuklu, O., Levin, D.A., and Austin, J.M., "Shock-shock interactions for a double wedge configuration in different gases," *Proceedings of the 53rd AIAA Aerospace Sciences Meeting*, AIAA-2015-0580, Kissimmee, FL, 2015.